Journal of the Meteorological Society of Japan

EARLY ONLINE RELEASE

The DOI for this manuscript is
DOI:10.2151/jmsj.2025-023
J-STAGE Advance published date: March 17, 2025
The final manuscript after publication will replace the preliminary version at the above DOI once it is available.

Identifying Cold Pool scales over Complex Topography using TaiwanVVM simulations

Po-Yen CHEN[1]

Department of Atmospheric Sciences, National Taiwan University, Taipei, Taiwan

and

Chien-Ming WU[1]

Department of Atmospheric Sciences, National Taiwan University, Taipei, Taiwan

August 20, 2024

----

1) Corresponding author: Chien-Ming Wu, Office, Department of Atmospheric Sciences, National Taiwan University, No. 1, Sec. 4, Roosevelt Road, Taipei, 10617 Taiwan.
Email: mog@as.ntu.edu.tw
Tel: +886-2-3366-3941

Abstract

In this study, our objective is to identify the appropriate cold pool scales over Taiwan's complex topography during predominant afternoon thunderstorms under a local-circulation dominated weather regime in summer. We utilize semi-realistic TaiwanVVM simulations, which cover the entire area of Taiwan, to investigate this phenomenon. Our findings reveal that when buoyancy is defined using a conventional environmental scale (109 km), the cold pool locations do not align with the precipitation areas, instead being concentrated mainly along the mountain ridges. We hypothesize that this discrepancy arises from the environmental scale at which cold pool buoyancy operates. To assess this, we conducted systematic analyses and the results show that an optimal environmental scale of approximately 7 to 11 km (about 3 times of the 75^{th} and 90^{th} percentile of the precipitation object length) can be identified. The statistics of cold pool frequency better align with precipitation hotspots, characterized by evaporative cooling over the plains and increased water loading within the core of precipitation objects over the mountains. We demonstrate that this method effectively captures the shift in cold pools associated with precipitation responses in a warming climate in Taiwan. This work highlights the importance of using an appropriate environmental scale when estimating buoyancy over complex topography.

Keywords cold pool; complex topography; buoyancy

1. Introduction

Diurnal convection over tropical islands is well known for its significant contribution to overall precipitation (Nesbitt and Zipser, 2003; Yang and Slingo, 2001). This convection is typically thermally driven and produces intense, short-duration heavy rainfall (Romatschke and Houze, 2011; X. Chen et al., 2015; Song and Zhang, 2020; Jian et al., 2021; P.-J. Chen et al., 2021; Krishna et al., 2021). In Taiwan, particularly over its complex topography, diurnal convection primarily occurs in the mountainous regions of southwest Taiwan, accounting for up to 40% of summer diurnal rainfall under local circulation-dominant conditions (Chang et al., 2023).

During convection development, the cold pool, driven by cold and dry downbursts from the cooling effect of precipitation evaporation (Doswell, 2001; Benjamin, 1968; Von Karman, 1940; Keulegan, 1957; Kuenen, 1950; Byers and Braham, 1949; Webster and Lukas, 1992), induces mechanical lifting for new convection initiation from the leading gust front (cold pool edge) (Droegemeier and Wilhelmson, 1985; Thorpe et al., 1982). The cold pool also triggers convection initiation from the surrounding cold pool under unstable atmospheric conditions (Tompkins, 2001a, 2001b). Moreover, convection initiation is more likely induced by cold pool collisions than by isolated cold pool lifting (Feng et al., 2015). Additionally, the collision of cold pools generated by convection with the sea-breeze front triggers new convection in the Taipei Basin (Kuo and Wu, 2019; Miao and Yang, 2020, 2022). This process demonstrates how cold pool dynamics extend convection development and influence its spatial distribution on tropical islands.

There are three primary methods used to identify cold pools. The buoyancy method involves the vertical integration of negative buoyancy derived from the density potential temperature (θ_v) anomaly (Schlemmer and Hohenegger, 2015; Tompkins, 2001a; Feng et al., 2015). The radial derivatives method identifies the cold pool edge by locating the steepest gradient of buoyancy (Drager and van den Heever, 2017). The radial gradient-based method identifies the cold pool edge where strong and narrow convergence regions exist near the surface (Fournier and Haerter, 2019; Henneberg et al., 2020).

The radial derivatives and radial gradient-based methods primarily identify the cold pool edge without considering the cold pool structure. In the radial gradient-based method, the surface convergence region calculated from near-surface wind is notably affected by steep terrain. Conversely, the buoyancy method not only identifies the cold pool edge but also characterizes the cold pool structure. This method can be used to explore the contribution of cold pools to the buoyancy structure near convective regions, which is related to the non-local effect in convection (Kuo and Neelin, 2022), particularly in diurnal convection over complex topography in Taiwan.

In our study, we quantify cold pools based on cold pool intensity (m s^{-1}) using the buoyancy method (Tompkins, 2001a; Feng et al., 2015). The buoyancy B is given by:

$$\mathrm{B} = \frac{\mathrm{g}(\theta_v - \bar{\theta}_v)}{\theta_{v_0}} \qquad \text{(Eqn. 1)}$$

$$\theta_v = \theta(1 + 0.608 q_v - q_l) \qquad \text{(Eqn. 2)}$$

$$\text{cold pool intensity} = \sqrt{-2\int_0^h \mathrm{B}dz} \quad \text{(Eqn. 3)}$$

where B is the buoyancy (m s^{-2}), g is the acceleration due to gravity (m s^{-2}), θ is the potential temperature, q_v is the mass mixing ratio of water vapor, and q_l includes cloud condensate water, rainwater, and ice. The θ_{v0} represents the reference state (Stevens, 2005, Yano et al., 2004). The $\overline{\theta}_v$ represents the θ_v average under conventional environmental scale (109km, the size of red box region in Fig.4a), which is used in previous studies (Feng et al., 2015)

The cold pool intensity is determined by integrating B from the point where it first exceeds -0.003 (m s^{-2}) (following Feng et al., 2015), which helps to estimate the cold pool depth (h) above the land surface. Fig. 1 shows the cold pool intensity in plain and mountainous regions from TaiwanVVM. However, the cold pool intensity is notably stronger and primarily concentrated near mountain ridges around 500 meters high, while it is nearly 0 m s^{-1} in the plains. The appropriate cold pool intensity for a tropical island is approximately 4 m s^{-1}(Drager & van den Heever, 2017; Zuidema et al., 2017).

In this study, we use the precipitation object length to determine the environmental scale, based on the concept that cold pools primarily occur near precipitation regions generated by convection. As the precipitation area increases, the area with cold pools also increases, indicating that the environmental field that can contain the negative buoyancy of the cold pool generated by convection also expands. Therefore, by using the precipitation area and expanding outward by a certain proportion as the environmental field for the negative buoyancy of the cold pool, we can identify the signals of cold pools generated near the convection. When the environmental scale is small, the resulting cold pools may be weak and fragmented, whereas when the environmental scale is large, the buoyancy calculation could be dominated by terrain surface heating/cooling or mountain-valley wind effects. In this study, we will identify an appropriate environmental scale for cold pools driven by convective precipitation over complex topography in Taiwan.

To investigate the relationship between cold pools and convection in complex terrain, we will calculate the statistics of diurnal precipitation objects. Cold pools formed by precipitation can trigger new convection, leading to convection merging process and stronger rainfall. Thus, cold pools not only initiate new convection but also act as a bridge in the process of convection merging, which is the primary scenario we studied. For large convection scales, the situation becomes more complex; for example, the lower atmosphere, influenced by heavy precipitation, becomes nearly saturated, and cold pools primarily form within the core of convective precipitation. Such scenario is beyond the scope of this study.

This study is organized as follows. Section 2 provides the model description and initial conditions of the TaiwanVVM ensemble member, and details of the Identification of the precipitation object length. Section 3 first presents the patterns of precipitation evolution in Taiwan under a local-circulation dominated weather regime, then examines the behavior of cold pool calculated from environmental scale structure and at last discuss the contribution on cold pool over complex topography in Taiwan. Section 4 discusses cold pool hotspot changes under Pseudo-Global Warming (PGW) scenario (Chen et al., 2024). The summary and conclusions are discussed in Section 5.

2. Data and Method

2.1 Model and experiment description

In this study, we use 30 cases of TaiwanVVM semi-realistic simulations as the member ensemble representing both the current and PGW climate, following Chang et al. (2021) and Chen et al. (2024). In the semi-realistic, the *realistic* aspect refers to the use of real topography and land-type distributions to construct the boundary conditions in the model to represent Taiwan island. Meanwhile, the *semi* aspect indicates that the atmospheric initial conditions are based on the 00Z Banqiao sounding data, assuming a horizontally homogeneous initial state which is typically used in Large-Eddy Simulations (LES). This setup focuses on the development of local circulation and convection-driven precipitation processes through surface boundary perturbations and differential heating caused by the terrain and land surface. TaiwanVVM (Wu et al., 2019) predicts the three-dimensional anelastic vorticity while the vertical velocity is diagnosed by solving a 3-D elliptic equation. The model uses predicted particle properties microphysics scheme (P3, Morrison and Milbrandt, 2015) and use the Rapid Radiative Transfer Model for GCMs (RRTMG; Iacono et al., 2008) as the radiative parameterization. To estimate the surface fluxes, the model uses the flux–profile relationship of Deardorff (1972), and the eddy viscosity and diffusivity coefficients depending on deformation and stability (Shutts and Gray,1994) as the first-order turbulence closure. TaiwanVVM includes realistic Taiwan orography (Wu and Arakawa, 2011) at 500m horizontal resolution and coupling Noah land surface model (Chen and Dudhia, 2001; Chen et al., 1996) version 3.4.1 to capture the differential surface heating over complex topography as the boundary conditions.

We adopted the definition of local-circulation dominated weather regime for the summer months (May to September) from 2005 to 2015 and selected 30 sounding dates as representative cases from Chang et al. (2021) as our TaiwanVVM simulation. The initial thermodynamic soundings (Fig. 2) represent a conditionally unstable environment typical of Taiwan's summer, which is the only difference among the simulations. This setup is to highlight the interactions between physical processes that control the development of local circulation and convection, as well as to examine the sensitivity of these processes to key environmental factors (Chen et al., 2024). The model setting of the whole cases we studied is in Table 1. For the discussion on cold pool frequency change, the PGW scenario is also considered.

2.2 Identification of the precipitation object length and environmental scale

The precipitation object length is determined by the precipitation object, which is connecting the raining grid points (≥ 5 mm h^{-1}) (Fig. 3a) in a two-dimensional (x-y) manner, following Tsai and Wu (2017). The precipitation object length (Fig. 3b) is calculated from the square root of the precipitation object's size, which also represents the convective scale in mountain region in Taiwan.

$$B = \frac{g(\theta_v - \tilde{\theta}_v)}{\theta_{v0}} \qquad \text{(Eqn.4)}$$

Next, eqn. (1) is modified from eqn. (4), where we $\bar{\theta}_v$ is $\tilde{\theta}_v$. Note that $\bar{\theta}_v$ is evaluated for the environmental scale of 109 km (red box region in Fig.4a), but $\tilde{\theta}_v$ is evaluated by using environmental scales that will be derived later. The $\tilde{\theta}_v$ is the horizontal average of θ_v calculated for the square domain with the edge length of an environmental scale. For example, the black box in Fig.3b which covers the precipitation object, is selected to calculate the local environmental state for convection developing under complex topography. In this study, we will evaluate the environment scale based on the precipitation object length. In each ensemble member, the precipitation object length is calculated based on four specific percentiles (25th, 50th, 75th, and 90th) (We will illustrate the meaning of choosing these percentiles in section 3.1) for each time period, reflecting the evolution of precipitation object length within the studied region. The selection of these percentiles aims to identify the precipitation object lengths at each time period in Southwest Taiwan.

3. Results

3.1 Overall Results

To understand the spatial distribution of precipitation object over southern Taiwan, we count the precipitation occurrence frequency where the rain rate is over 5 mm h^{-1}. The result shows that precipitation mainly occurs in the southwestern mountain hill (500-1500 m) and high mountain (>1500 m) regions (Fig. 4a). Within this area, the highest precipitation frequency is primarily found in the mountain hill region, with a frequency of about 10-15%, indicating a precipitation hotspot. Based on this result, the following study focuses on the terrestrial region inside the red box in Fig. 4a. We hypothesize that the precipitation hotspots are caused by sea-breeze inflow in the plain region (<500 m) and mountain winds from surface heating or downbursts driven by convection in the high mountain region. To verify this hypothesis, we analyze the mean precipitation evolution in three studied terrains: plains, mountain hills, and high mountains.

To further understand when the precipitation mainly occurred, we analyze the precipitation evolution in plain, mountain hill and high mountain regions. The result shows that the time offset of the mean precipitation peak reflects the convection development in these area (Fig. 4b). The earliest and most intense precipitation peak among the three areas occurs in the high mountain region (2.1 mm h^{-1}) around 14 LST, and it decreases until 21 LST. In the plain region, the mean precipitation slightly increases by 0.1 mm h^{-1} at 16 LST, likely due to the convective system developing from the mountain hill region, where the mean precipitation around 16 LST is still increasing.

In the plain region, precipitation before the diurnal peak at 15:30 LST, with a diurnal amplitude of about 0.5 mm h^{-1}, which is much smaller than in other regions. In the mountain hill region, the diurnal peak of mean precipitation is 1.9 mm h^{-1} around 16 LST, which is delayed by about 2 hours compared to the high mountain region and 0.5 hours compared to the plain region. We infer that the additional forcing comes from mountain winds and outflows from the high mountain region, as well as the sea-breeze inflow from the plain region. After 16 LST, the mean precipitation in the mountain hill region was 0.25 mm h^{-1} and 0.5-1.5 mm h^{-1} greater than in the high mountain and plain regions, respectively. The mean precipitation remains higher in the mountain hill region than in the other two regions until night, with less surface heating from 17 to 21 LST. This highlights the persistence of convection and the precipitation hotspot (Fig. 4a), which we infer is due not only to the additional forcing from the high mountain and plain regions but also to the interactions of local convection with cold pools and surface inflow over the complex topography, maintaining the precipitation events in the mountain hill region.

From Fig. 4c, the result shows that the diurnal peak of largest 90th precipitation object length is about 5.5 km, which reveals that the scale of the afternoon thunderstorm in Taiwan is small. To identify the location of such precipitation objects, we label the most frequent occurrence altitude among ensemble members using symbols: circles for below 500 m, squares for 500–1500 m, and triangles for above 1500 m, respectively. The square on the lines shows that the precipitation object, which the convection mainly occurs in mountain hill region after 14 LST until night (21 LST). In 75th to 90th percentile, the diurnal peak is about 3.2 to 5.5 km, and the diurnal variation is larger (about 1.7 to 3.5 km) than in 25th and 50th (smaller than 0.5 km), means that the object length in 75th and 90th percentile relatively reflects the diurnal variation of convection. The analysis of precipitation object length reveals that the scale of afternoon thunderstorms in Taiwan is generally small, even at the 90th percentile. This suggests that, due to constraints imposed by the complex topography, the environmental scale of cold pools must be larger than the precipitation object but small enough to avoid interference from the terrain. Therefore, we will design systematic analyses based on the length scales obtained in this section as a guide to evaluate how to select an appropriate environmental scale over complex terrain.

3.2 The analysis of environmental scale for cold pool

Based on the precipitation object analysis in Section 3.1, we will test the environmental scale using the diurnally averaged 25th, 50th, 75th, and 90th percentiles of precipitation object lengths, which are 0.88, 1.48, 2.42, and 3.67 km, respectively. By extending these spatial scales outward by an additional factor of the object length on all sides, we select three times the original scale, which is large enough to cover the precipitation objects, resulting in 2.66, 4.44, 7.25, and 11.01 km, respectively. This approach will help determine the lower bound of the environmental scale. Additionally, we extend the scale by incorporating larger environmental scales—33 km, 66 km, 89 km and 100 km—to determine the upper bound, which is constrained by the spatial scale of the terrain. This methodology allows us to evaluate the environmental scale that can be applied to other tropical islands with complex topography.

It is important to note that cold pool calculations will be excluded if the ratio of missing grid points (e.g., due to terrain) to total grid points within the environmental scale domain exceeds 0.5 for a specific land surface point (i.e., the black point in Fig. 3b).

To clearly illustrate the contrast in cold pool distribution at different scales, Fig. 5 presents results for four selected scales (2.66 km, 7.25 km, 33 km, and 89 km, respectively) and focuses on the plain and mountain regions in one of the ensemble members. The environmental scale is represented as a range, as the results between the 25th and 50th percentiles are similar, while those between the 75th and 90th percentiles are also comparable. For simplicity, these ranges are referred to as 2–4 km and 7–11 km, respectively. Similarly, the results between 33 km and 60 km are comparable, as are those between 89 km and 100 km. For simplicity, these ranges are referred to as 33–60 km and 89–100 km, respectively.

Figs. 5a and b show that with a small environmental scale (2–4 km), the cold pool distribution shows weak signals surrounding the precipitation region in both plain and mountainous areas. Even though the cold pool distribution exhibits a gust-front-like structure, it is severely fragmented and appears as only a surface perturbation in the precipitation region. This indicates that the scale is too small, capturing only grid-point scale negative buoyancy signals and failing to show the cold pool structure driven by the local convective system.

With a larger environmental scale of approximately 7–11 km, the cold pool structure forms a well-defined ring structure with an appropriate cold pool intensity of approximately 4 m s^{-1} in the plain region (Fig. 5c). In the mountain region (Fig. 5d), where the terrain is divided, the cold pool structure from large convective systems cannot form a complete ring structure. Currently, the main focus is on observing the cold pools generated by convection before the convective cells merge and grow, which subsequently trigger new convection and aid in further process of convection merging. The identified environmental scale ranges in 7–11 km, and the calculated cold pool signals mainly reflect the precipitation objects that contain a single stronger precipitation core. In precipitation objects larger than 20 km, even when using an environmental scale of 7–11 km to calculate the cold pool, it reflects the cold pool signals generated around the stronger precipitation cores within the precipitation objects.

When the environmental scale increases to 33-60 km, the cold pool intensity becomes excessively strong, and the structure starts to become vague and mismatches with the precipitation region in the plain region (Fig. 5e). In the mountain region (Fig. 5f), although some of the cold pool distribution concentrates in the precipitation region similar to Fig. 5d, it follows the mountain ridge without aligning with the precipitation region. Furthermore, the cold pools within strong precipitation areas are primarily distributed within larger precipitation objects without extending outward. It is hypothesized that the likelihood of triggering new convection is lower (since the surrounding environment is within smaller precipitation areas). Additionally, at this environmental scale, larger-scale environmental signals such as orographic cooling or valley winds may also be reflected in the cold pool signals. When the environmental scale is near the conventional value (89–100 km) (Figs. 5g and h), the cold pool intensity becomes weaker (<1 ms^{-1}) in the plain region and excessively strong (>5 ms^{-1}) in the mountain region, which does not align with the precipitation patterns shows in Fig.

1.

To sum up, from the cold pool distribution under the environmental scale from 2–4 to 89–100 km, we selected environmental scale in the range of 7–11 km as the appropriate environmental scale in southwest Taiwan.

To demonstrate that the cold pool distribution is reasonable based on the precipitation within our selected scales, we calculate the cold pool frequency distribution across ensemble members. From Fig. 6a, which is the cold pool calculated from the environmental scale in 7–11 km, the result shows that cold pool mainly occurred at the near-mountain region, where is the precipitation region. And in Fig. 6b, the cold pool frequency distribution using 89–100 km environmental scale shows that the cold pool mainly occurs in the coastal and high mountain regions, which is without obvious precipitation occurred. These high frequency regions of cold pool are due to the larger environmental and terrain cooling features and cause the bias. From the statistic of frequency, the cold pool calculated from the environmental scale in 7–11 km relatively better reflects the precipitation region. In addition, within the environmental scale of 7–11 km, the cold pool distribution not only concentrates near the mountainous region (500 m-1500 m altitude), which is close to the high-precipitation area shown in Fig. 4a, but also exhibits a clear line structure extending from the coastline to the inland. We infer that the cold pool signal results from different contributions to the negative buoyancy near the surface. We will further discuss the buoyancy contribution in the next subsection.

3.3 Contribution for the negative buoyancy in cold pool

The cold pool intensity in this study is calculated based on buoyancy, which is the density potential temperature (θ_v) anomaly (Eqn.4). There are three terms contributing to θ_v (Eqn.2): potential temperature, water vapor, and liquid water loading (i.e., cloud, ice, and rainwater). To analyze the contribution from these three terms individually, we follow the linearized buoyancy equation in Wilhelmson and Ogura (1972), and Grabowski and Morrison (2021) below:

$\mathrm{B} = \mathrm{g}\left(\frac{\theta'}{\theta_0} + 0.608q'_v - q_l\right)$ (Eqn. 5), where

$\theta' = \theta - \tilde{\theta},\ q'_v = q_v - \tilde{q}_\mathrm{v}$, the tilde term ($\sim$) is the spatial averaged with the environmental scale domain. The θ_0 represents the reference state (Stevens, 2005, Yano et al., 2004). From the linearized buoyancy equation, it shows the negative buoyancy contribution in cold pools comes from negative potential temperature anomaly ($\frac{\theta'}{\theta_0}$), reduced water vapor (0.608 q'_v), and increased liquid water loading (-q_l). The negative potential temperature anomaly is mainly from the evaporative cooling (roughly 2 order larger than radiative cooling in our study) near the precipitation region under the environmental scale in 7–11 km. We use evaporative cooling to refer to the effect caused by the negative potential temperature anomaly.

In Fig. 7, we calculate the cold pool contributions from these three terms for environmental scale of 7.25 km. To discuss the spatial distribution of precipitation regions and the contributions from the three terms to the cold pool and precipitation, we use three precipitation thresholds to represent the regions with precipitation intensity above light rainfall (5 mm h^{-1}, red solid contour), moderate rainfall (15 mm h^{-1}, red dashed contour), and heavy rainfall (50 mm h^{-1}, green contour). The contribution to cold pool intensity from evaporative cooling (Figs.7a and b) are roughly similar to those from increased liquid water loading (Figs.7c and d), while the contribution from reduced water vapor (Figs.7e and f) is the smallest among the three; however, they have different spatial distribution over plain and mountain regions. Fig.7a shows that in the plain region, the cold pool contribution from evaporative cooling is mainly distributed around the regions above moderate rainfall intensity, while the cold pool intensity over the regions above light rainfall is relatively less pronounced. Fig. 7b shows that, in the mountainous region (X = 3–5 km), the cold pool caused by evaporative cooling is also primarily distributed around the moderate precipitation region. However, the cold pool intensity resulting from evaporative cooling in the mountainous region is weaker than that in the plain regions. A possible reason for this is the higher temperature in plains compared to mountains, which results in a higher saturation vapor pressure over plains. Consequently, the amount of water vapor available for evaporation is greater in plains than in mountainous areas. As a result, evaporative cooling is more effective in plains, leading to the formation of stronger cold pools compared to those in mountainous regions. Fig.7c shows that the cold pool caused by increased liquid water loading is primarily distributed within the center of the region above moderate rainfall intensity. In Fig.7d, in the vicinity of the mountain hill region, the cold pool caused by increased liquid water loading distribute within both the moderate precipitation region (X =

3–5 km) and the heavy precipitation regions within the mountain hill area (X = 18–20 km, Y = 8–15 km, and X = 15 km, Y = 22 km). In Figs.7e and 7f, the distribution of the cold pool contribution from water vapor does not exhibit clear relationship with the precipitation regions either in the plain or mountainous areas, and its overall intensity remains relatively weak (<1 m s^{-1}). These results indicate that the cold pool associated with precipitation over Taiwan's plains and mountainous regions is primarily driven by evaporative cooling and increased liquid water loading.

To demonstrate the statistics of the cold pool from the three terms (evaporative cooling, liquid water loading, and water vapor) in Southwestern Taiwan across all ensemble members, we define the cold pool intensity greater than or equal to 1 m s^{-1} as cold pool occurred. In Fig.8a, the result shows that the cold pool caused by evaporative cooling is mainly distributed in the mountain hill region and the plains near the mountain hill region. This may be due to the cold pool generated by evaporative cooling from convective precipitation, triggered when the sea breeze advances toward the mountain hill region in our simulation. The broader distribution of the cold pool in this area might be related to the widespread occurrence of convection in the plains near the mountainous region.

Next, the cold pool from the increased liquid water loading shows that the cold pool caused by increased liquid water loading is primarily distributed in the mountain hill and high mountain regions (Fig.8b). This distribution is associated with intense precipitation occurring in these mountainous areas. However, due to the smaller spatial extent of intense precipitation, the frequency and spatial coverage of this cold pool are relatively smaller and less frequent compared to those caused by evaporative cooling.

Finally, the cold pool contributed from reduced water vapor is mainly distributed over the coastal plains (Fig.8c). And it roughly shows a distinct north-south boundary with the cold pool contributed from evaporative cooling (Fig.8a). The cold pool contributed from reduced water vapor may be due to local subsidence, in addition to the sea-breeze inflow, forming Horizontal Convective Rolls (HCR) (Dailey and Fovell, 1999) before the convective precipitation initiated from sea-breeze front and surface heating. This local subsidence brings relatively dry air with less water vapor, contributing to negative buoyancy in this region. While the cold pool contributions from water vapor induce some convection in the plain region, the intensity and occurrence are too small to be significant in our study.

Based on the results from different environmental scales and cold pool contributions, it is shown that the 7–11 km environmental scale can accurately reflect the cold pool distribution over Taiwan's complex topography. In Section 3.4, we evaluate the cold pool structure over this complex terrain by examining the evolution of the cold pool and convection in a cross-sectional view of the mountainous region.

3.4 The evolution of cold pool and the convection interaction in mountain region

To demonstrate the evolution and interaction between the cold pool and convection over Taiwan's complex topography, we evaluate the cold pool's development and its interaction with convection and near-surface inflow in the mountainous region. As indicated by the cold pool evolution over a time interval from 14:40 to 15:00 LST (Figs. 9a to c), the cold pool and convection together induce lower boundary updrafts in less than 10 minutes, with the cold pool providing more convection triggering than the terrain. Additionally, the evolution shows that these updrafts (seen as new convection initiations) generate new cold pool signals, which can then induce updrafts in other locations.

We use vertical cross-section diagrams to illustrate the interactions among cold pools, convection, inflows, and terrain. These processes occur on a short convective timescale, with significant changes happening within approximately 20 minutes. In Fig. 9d (14:40), at around 10 km, the inflow collides with the leading edge of the cold pool near the mountain slope from the previous time step, triggering an updraft. This process exemplifies how the cold pool edge leads to new convection. Simultaneously, at around 18 km, a downburst generated by precipitation interacts with the outflow from the convection at 10 km. Ten minutes later (14:50, see Fig. 9e), convection and precipitation occur at around 15 km, accompanied by a negative θ_v' signal at a height of 1–1.5 km, indicating cooling of about 0.1–0.3 K. This process maintains the cold pool's presence below (X=12–15 km).

From 14:50 to 15:00, precipitation shifts to steeper terrain at horizontal positions of 15–17 km. The accompanying cold pool accumulates along the mountain slope, inducing localized updrafts at 15 km and cold pool heights between 1.5 and more than 2 km, with vertical velocities reaching approximately 1 m s^{-1}. These results demonstrate that the cold pools defined in this study over complex terrain exhibit preliminary evidence of interactions among inflows, convection, cold pools, and terrain on small horizontal scales (approximately 5 km) and short timescales (10–20 minutes). This provides a foundation for future research on the physical processes of convection and cold pools in complex terrain.

4. Implication of cold pool hotspot changes under global warming

From the previous analysis, we identified an appropriate environmental scale (7–11 km) for the cold pool calculation over Taiwan's complex terrain. To highlight the advantages of our cold pool definition compared to the conventional scale (89–100 km), we used the cold pool defined by these two scales to analyze the afternoon thunderstorm simulations in TaiwanVVM. We then compared the changes in cold pool distribution between the current and PGW scenarios.

Based on Chen et al. (2024), where 30 ensemble members are simulated under local-circulation-dominated weather patterns during summer, the PGW scenario assumes an increase of 3 K in the entire atmospheric temperature (while maintaining the same relative humidity) compared to the current climate. In the current climate scenario, the precipitation hotspot is primarily concentrated in the mountainous region, as discussed in Section 3.1. Under the PGW scenario, the precipitation hotspot expands to the plains (Fig. 10a). The transition from the current climate to the PGW scenario shows the precipitation hotspot shifting from the mountainous region (Fig. 4a) to plain area near the mountains (Fig. 10b), with a frequency increase of up to 9%.

Under the PGW scenario, the cold pool calculated using the 7-11 km environmental scale shows a frequency distribution pattern (Fig. 10c) similar to that of the current climate (Fig. 6a). The difference in cold pool frequency between the current and PGW scenarios (Fig. 10d) shows an overall increase in frequency, with a greater concentration over the plain areas near the mountains compared to the mountainous regions. The cold pool frequency increases by approximately 9% in the corresponding regions. However, when the conventional environmental scale is used, the pattern of cold pool frequency distribution becomes less distinct (Fig. 10e), with differences of up to 20%, primarily reflecting cold pools driven by land, sea, and mountain-scale forcing (Fig. 10f). This preliminary diagnosis opens up future applications for studying convection–cold pool interactions over complex topography, which could contribute to longer and stronger convective lifetimes and intensities, as discussed in Chen et al., 2024.

5. Summary and Conclusions

This study investigates the identification of appropriate cold pool scales over Taiwan's complex topography, particularly during prevalent afternoon thunderstorms under a local-circulation dominated weather regime in summer. Using semi-realistic TaiwanVVM simulations covering the entire Taiwan, we identify the appropriate environmental scale for calculating cold pools. We hypothesize that the environmental scale should be large enough to cover the precipitation object while remaining small enough to avoid interference from land, sea, and mountain distributions. Our analysis identifies an optimal environmental scale of approximately 7–11 km, corresponding to three times the precipitation object length between the 75th and 90th percentiles. This newly identified environmental scale better captures the cold pool frequency distribution in relation to precipitation hotspots, with cold pools characterized by evaporative cooling over plain area near the mountains and increased water loading over mountainous areas. We also demonstrate that cold pool interactions associated with topography can be clearly identified using this definition.

In conclusion, this study provides a new insight into identify the cold pool over complex topography in Taiwan through the environmental scale about 7–11 km based on the relationship with the precipitation object of afternoon thunderstorm. The selection of such an environmental scale for other tropical islands can follow our approach by first identifying the dominant precipitation object scale, then systematically increasing it to the conventional environmental scale to determine the optimal scale which further studies of cold pool related processes.

Data Availability Statement

The data that support the findings of this study are available on request from the corresponding author.

Acknowledgement

This work was supported by the National Science and Technology Council of Taiwan through Grants NSTC112-2123-M-002-006, NSTC113-2111-M-002-001, NSTC113-2111-M-002-013, NSTC113-2111-M-002-001-, and National Taiwan University Grants NTU-

112L7832 and NTU-112L7858. The authors sincerely thank the National Center for High-performance Computing (NCHC) for providing the high-performance computation platform to conduct the simulation

References

Benjamin, T. B., 1968: Gravity currents and related phenomena. Journal of Fluid Mechanics, **31(2)**, 209–248

Bjorn Stevens, 2005: ATMOSPHERIC MOIST CONVECTION https://doi.org/10.1146/annurev.earth.33.092203.122658

Byers, H. R., & Braham, R. R., 1949: The thunderstorm: Report of the thunderstorm project. Washington, DC: US Government Printing Office.

Chang, Y.-H., Chen, W.-T., Wu, C.-M., Moseley, C., and Wu, C.-C., 2021: Tracking the influence of cloud condensation nuclei on summer diurnal precipitating systems over complex topography in Taiwan, Atmos. Chem. Phys., **21**, 16709–16725, https://doi.org/10.5194/acp-21-16709-2021

Chang Y-H, Chen W-T, Wu C-M, Kuo Y-H and Neelin, J-D, 2023: Identifying the deep553 inflow mixing features in orographically-locked diurnal convection Geophys **554** Res. Lett. 50 e2023GL103107

Chen, F. and Dudhia, J. 2001: Coupling an Advanced Land Surface–Hydrology Model with the Penn State–NCAR MM5 Modeling System. Part I: Model Implementation and

Sensitivity, Mon.Weather Rev., **129**, 569–585, doi:10.1175/1520-0493(2001)129<0569:Caalsh>2.0.Co;2.

Chen, F., Mitchell, K., Schaake, J., Xue, Y., Pan, H.-L., Koren, V., Duan, Q. Y., Ek, M., and Betts, A., 1996: Modeling of land surface evaporation by four schemes and comparison with FIFE observations, J. Geophys. Res.-Atmos., **101**, 7251–7268,doi:10.1029/95jd02165.

Chen, P.-J., Chen, W.-T., Wu, C.-M., & Yo, T.-S., 2021: Convective cloud regimes from a classification of object-based CloudSat observations over Asian-Australian monsoon areas. Geophysical Research Letters, **48(10)**, e2021GL092733. https://doi.org/10.1029/2021GL092733

Chen, W.-T., Y.-H. Chang, C.-M. Wu, H-Y. Huang, 2024: The future extreme precipitation systems of orographically locked diurnal convection: The benefits of using large-eddy simulation ensembles, Environmental Research: Climate. https://doi.org/10.1088/2752-5295/ad557d

Chen, X., Zhao, K., Xue, M., Zhou, B., Huang, X., & Xu, W., 2015: Radar-observed diurnal cycle and propagation of convection over the Pearl River Delta during Mei-Yu season. Journal of Geophysical Research: Atmospheres, **120(24)**, 12557–12575. doi:10.1002/2015JD023872

Dailey, P.S., Fovell, R.G., 1999: Numerical simulation of the interaction between the sea-breeze front and horizontal convective rolls. Part I: offshore ambient flow. Mon. Weather

Rev. **127 (5)**, 858–878. https://doi.org/10.1175/1520-0493(1999)127<0858:nsotib>2.0.co;2.

Doswell, C. A., 2001: Severe convective storms—An overview. In C. A. Doswell (Ed.), Severe convective storms, Meteorological Monographs. Boston, MA: American Meteorological Society.

Drager, A. J., & van den Heever, S. C., 2017: Characterizing convective cold pools. Journal of Advances in Modeling Earth Systems, **9**, 1091–1115. https://doi.org/10.1002/2016MS000788

Droegemeier, K. K., & Wilhelmson, R. B., 1985: Three-dimensional numerical modeling of convection produced by interacting thunderstorm outflows. Part I: Control simulation and low-level moisture variations. Journal of the Atmospheric Sciences, **42(22)**, 2381–2403.

Feng, Z., Hagos, S., Rowe, A. K., Burleyson, C. D., Martini, M. N., & de Szoeke, S. P., 2015: Mechanisms of convective cloud organization by cold pools over tropical warm ocean during the AMIE/DYNAMO field campaign. Journal of Advances in Modeling Earth Systems, **7**, 357–381. doi:10.1002/2014MS000384

Fournier, M. B., & Haerter, J. O., 2019: Tracking the gust fronts of convective cold pools. Journal of Geophysical Research, **124**, 11,103–11,117. https://doi.org/10.1029/2019JD030980

Henneberg, O., Meyer, B., & Haerter, J. O., 2020: Particle-based tracking of cold pool gust fronts. Journal of Advances in Modeling Earth Systems, **12**, e2019MS001910.

https://doi.org/10.1029/2019MS001910

Jian, H.-W., Chen, W.-T., Chen, P.-J., Wu, C.-M., & Rasmussen, K. L., 2021: The synoptically-influenced extreme precipitation systems over Asian-Australian monsoon region observed by TRMM precipitation radar. Journal of the Meteorological Society of Japan, **99(2)**, 269–285. https://doi.org/10.2151/jmsj.2021-013

Jun-Ichi Yano, Jean-Pierre Chaboureau, Françoise Guichard, 2005A: A generalization of CAPE into potential-energy convertibility. https://doi.org/10.1256/qj.03.188

Keulegan, G., 1957: An experimental study of the motion of saline water from locks into fresh water channels (Technical Report 5168): National Bureau of Standards.

Krishna, U. V. M., Das, S. K., Deshpande, S. M., & Pandithurai, G., 2021: Physical processes controlling the diurnal cycle of convective storms in the Western Ghats. Scientific Reports, **11(1)**, 14103. doi:10.1038/s41598-021-93173-0

Kuenen, P. H., 1950: Turbidity currents of high density. 18th International Geological Congress (1948) (Vol. 8). London. Reports, pt.

Kuo, K.-T., and C.-M. Wu, 2019: The precipitation hotspots of afternoon thunderstorms over the Taipei basin: Idealized numerical simulations. J. Meteor. Soc. Japan, **97**, 501–517.

Kuo, Y.-H., & Neelin, J. D., 2022: Conditions for convective deep inflow. Geophysical Research Letters, **49**, e2022GL100552. https://doi.org/10.1029/2022GL100552

Miao, J.-E., and M.-J. Yang, 2020: A Modeling Study of the Severe Afternoon

Thunderstorm Event at Taipei on 14 June 2015: The Roles of Sea Breeze, Microphysics, and Terrain. J. Meteor. Soc. Japan, **98**, 129-152.

Miao, J.-E., and M.-J. Yang, 2022: The Impacts of Midlevel Moisture on the Structure, Evolution, and Precipitation of Afternoon Thunderstorms: A Real-Case Modeling Study at Taipei on 14 June 2015. J. Atmos. Sci., **79**, 1837–1857.

Nesbitt S-W and Zipser E-J, 2003: The diurnal cycle of rainfall and convective intensity according to three years of TRMM measurements J. Clim. **16** 1456-1475

Romatschke, U., & Houze, R. A., 2011: Characteristics of precipitating convective systems in the South Asian monsoon. Journal of Hydrometeorology, **12(1)**, 3–26. https://doi.org/10.1175/2010JHM1289.1

Schlemmer, L. and Hohenegger, C., 2015: Modifications of the atmospheric moisture field as a result of cold-pool dynamics, Q. J. Roy. Meteor. Soc., **142**, 30–42, https://doi.org/10.1002/qj.2625.

Song, Z., & Zhang, J., 2020: Diurnal variations of summer precipitation linking to the topographical conditions over the Beijing-Tianjin-Hebei region. Scientific Reports, **10(1)**, 9701. https://doi.org/10.1038/s41598-020-65743-1

Thorpe, A., Miller, M., & Moncrieff, M., 1982: Two-dimensional convection in non-constant shear: A model of mid-latitude squall lines. Quarterly Journal of The Royal Meteorological Society, **108(458)**, 739–762.

Tompkins, A. M., 2001a: Organization of tropical convection in low vertical wind shears:

The role of cold pools. Journal of the Atmospheric Sciences, **58(13)**, 1650–1672.

Tompkins, A. M. (2001b). Organization of tropical convection in low verticalwind shears: The role ofwater vapor. Journal of the atmospheric sciences, **58(6)**, 529–545.

Tsai, W.-M., and C.-M. Wu, 2017: The environment of aggregated deep convection, J. Adv. Model. Earth Syst., **9**, 2061–2078, doi:10.1002/2017MS000967.

Von Karman, T., 1940: The engineer grapples with nonlinear problems. Bulletin of the American Mathematical Society, **46(8)**, 615–683.

Wilhelmson, R., and Y. Ogura, 1972: The Pressure Perturbation and the Numerical Modeling of a Cloud. J. Atmos. Sci., 29, 1295–1307, https://doi.org/10.1175/1520-0469(1972)029<1295:TPPATN>2.0.CO;2.

Webster, P. J., & Lukas, R., 1992: TOGA COARE: The coupled ocean–atmosphere response experiment. Bulletin of the American Meteorological Society, **73(9)**, 1377–1416.

Wojciech W. Grabowski and Hugh Morrison, 2021: Supersaturation, buoyancy, and deep convection dynamics https://acp.copernicus.org/articles/21/13997/2021/#section13

Wu C-M and Arakawa A, 2011: Inclusion of surface topography into the vector vorticity equation model (VVM) J. Adv. Model. Earth Syst. 3 M04002

Wu C-M, Lin H-C, Cheng F-Y and Chien M-H, 2019: Implementation of the land surface processes into a vector vorticity equation model (VVM) to study its impact on afternoon thunderstorms over complex topography in Taiwan Asia-Pac. J. Atmos. Sci. **55** 701-717

Yang G-Y and Slingo J, 2001: The diurnal cycle in the tropics Mon. Weather Rev. **129** 725 784-801

Zuidema, P., Torri, G., Muller, C., & Chandra, A., 2017: A survey of precipitation-induced atmospheric cold pools over oceans and their interactions with the larger-scale environment. Surveys in Geophysics, **38(6)**, 1283–1305.

List of Figures

Fig. 1 The cold pool intensity (blue shading, m s^{-1}) is calculated using the conventional environmental scale (109km, red box in Fig. 4), shown alongside the precipitation region (red contour, 5 mm h^{-1}) and near-surface wind (purple vectors) in the (a) plain and (b) mountainous regions. The terrain is represented by grey shading.

Fig. 2 The initial profiles of equivalent potential temperature and saturated equivalent potential temperature for the current and PGW scenarios. Solid lines represent the current scenario, and dashed lines represent the PGW scenario. Red lines indicate equivalent potential temperature, and green lines indicate saturated equivalent potential temperature. Thick lines represent the mean initial soundings, while thin lines represent 30 initial soundings. In Current and the PGW scenario, the mean lifting condensation level (LCL) are both 960hPa, level of free convection (LFC) are 820 and 840hPa. The convective inhibition (CIN) are 55 and 45 Jkg^{-1}, and the convective available potential energy (CAPE) are 1600 and 3200 Jkg^{-1}, respectively.

Fig. 3 Schematic diagram of the precipitation object length. (a) shows a color-shaded snapshot of the precipitation rate in the mountainous region for one ensemble member during the afternoon, while (b) shows the corresponding snapshot of the precipitation object length at the same time. The grey shading represents the terrain, with black contours indicating altitudes of 0, 500, and 1500 meters. The edge length of the black box represents the environmental scale (approximately 10 km), based on three times the 75th and 90th percentile of the precipitation object length at the same time and for the same ensemble member. The value of $\tilde{\theta}_v$ is the horizontally averaged potential temperature within the black box region, centered at the black point.

Fig. 4 (a) The frequency (%) of precipitation exceeding 5 mm h^{-1} (shaded), based on statistics from 14 to 21 LST across 30 ensemble members. Black contours represent altitudes of 0, 500, and 1500 meters. The red box highlights the study region with relatively high precipitation frequency. (b) The precipitation evolution in three sea-level height regions (below 500 m, 500–1500 m, and above 1500 m) within the red box from (a). The line represents the mean, and the shaded area indicates one standard deviation of precipitation across 30 ensemble members. (c) The evolution of precipitation object length over four percentiles (25th, 50th, 75th, 90th) per time period for each ensemble member. The line represents the mean, and the shaded area indicates one standard deviation of precipitation object length across 30 ensemble members. The markers indicate different sea-level height regions where the mode of precipitation object centers falls within the four percentiles across all 30 ensemble members. Dots represent areas below 500 m (plain), squares correspond to regions between 500 and 1500 m (mountain hill region), and triangles denote areas above 1500 m (high-mountain region).

Fig. 5 The precipitation at rates of 5, 15, and 50 mm h^{-1} (red solid, red dashed, and green solid contours, respectively) and cold pool intensity (blue shading, unit: m s^{-1}) calculated using different environmental scales in the plain (a, c, e, g) and mountainous (b, d, f, h) regions for one ensemble member. Grey shading represents sea-level height (in meters).

Fig. 6 The occurrence frequency map of cold pools under the appropriate environmental scale of (a) 7–11 km and (b) 89–100 km during 14–21 LST. Frequency is defined by the number of occurrences where cold pool intensity is ≥ 1 m s^{-1}. Contours represent altitudes of 0, 500, and 1500 meters.

Fig. 7 The negative buoyancy contribution to the cold pool, under the appropriate environmental scale (7–11 km, represented here by a scale of 7.25 km), is shown in Figs. 5c and 5d for the plain (a, c, e) and mountainous (b, d, f) regions. Panels (a, b), (c, d), and (e, f) correspond to the contributions from evaporative cooling, increased liquid water content loading, and reduced water vapor effects, respectively. Precipitation rates of 5, 15, and 50 mm h^{-1} are shown with red solid, red dashed, and green solid contours, respectively, while cold pool intensity is shown in blue shading (unit: m s^{-1}). Grey shading represents altitude (in meters).

Fig. 8 The occurrence frequency map of cold pools driven by negative buoyancy contributions from (a) evaporative cooling, (b) increased liquid water loading, and (c) reduced water vapor under the appropriate environmental scale (7–11 km) during 14–21 LST. Frequency is defined by the number of occurrences where cold pool intensity is ≥ 1 m s^{-1}. Contours represent altitudes of 0, 500, and 1500 meters, respectively.

Fig. 9 The evolution of the horizontal (a–c) and vertical cross-section (d–f) from 14:40 to 15:00 LST with the cold pool calculated using the 7–11 km environmental scale. In the upper panel (a–c), grey shading represents sea-level height (m), blue shading shows cold pool intensity (m s^{-1}), and the red contour marks the updraft region where vertical velocity is 1 m s^{-1} at a 1 km height. In the lower panel (d–f), the vertical cross-section follows the black dashed line in (a–c), oriented from Northwest to Southeast. In the upper portion of (d–f), green bars represent terrain height (km), blue line indicates cold pool height (km), purple shading denotes the negative θ'_v, which is $(\theta_v - \tilde{\theta}_v)$ (K). Black contour represents where the combined cloud water and ice water mixing ratio higher than 0.01 g kg^{-1}, and bright shading highlights rainwater regions where the mixing ratio exceeds 0.5 g kg^{-1}. Purple vectors represent the horizontal wind anomaly, calculated by subtracting the horizontal wind at X = 0 km (sea-breeze inflow) from the original wind field, and are projected along the dashed line. These vectors are combined with vertical wind (m s^{-1}), while red vectors highlight vertical winds exceeding 1 m s^{-1}. The red contour represents a region where the updraft velocity is higher than 3 m s^{-1}. In the lower portion, blue bars depict cold pool intensity (m s^{-1}), and the green line represents precipitation rate (mm h^{-1}).

Fig. 10 The occurrence frequency map from 14:00 to 21:00 LST for precipitation (a, b) and cold pools under environmental scales of 7–11 km (c, d) and 89–100 km (e, f) in the PGW scenario, along with the difference between the two scenarios (PGW - current). Frequency is defined by the number of occurrences where cold pool intensity is ≥ 1 m s^{-1}. Black contours represent altitudes at 0, 500, and 1500 meters, respectively.

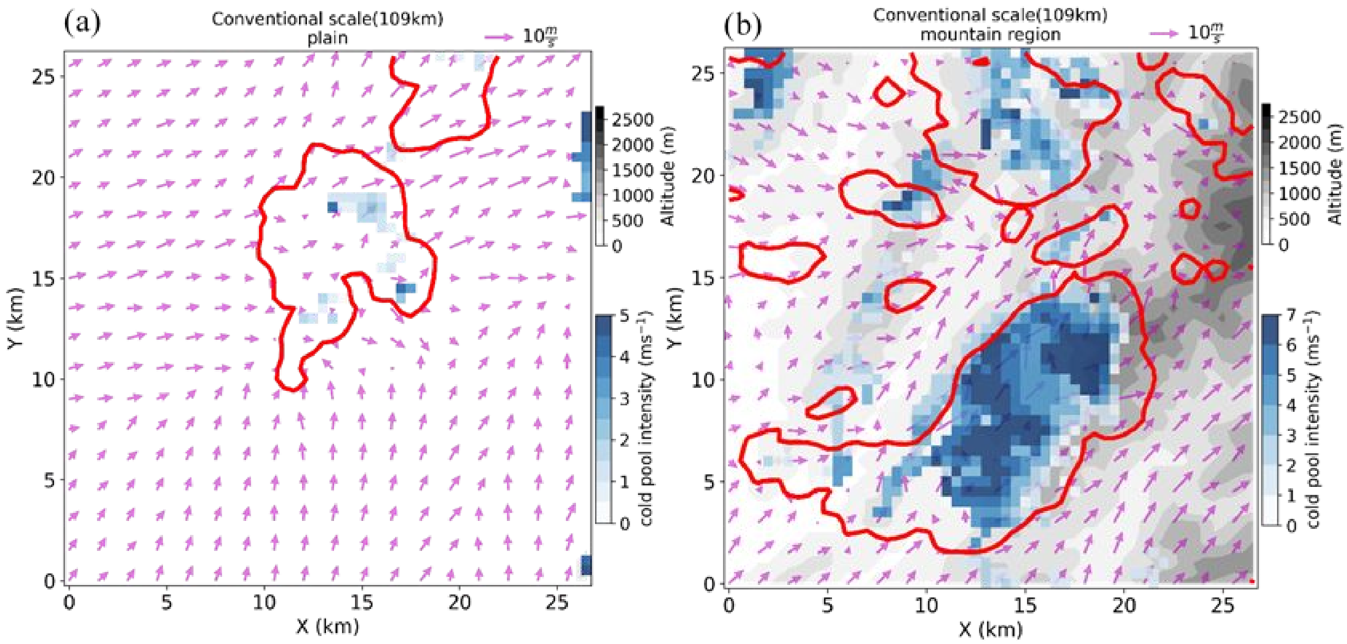

Fig. 1 The cold pool intensity (blue shading, m s^{-1}) is calculated using the conventional environmental scale (109km, red box in Fig. 4), shown alongside the precipitation region (red contour, 5 mm h^{-1}) and near-surface wind (purple vectors) in the (a) plain and (b) mountainous regions. The terrain is represented by grey shading.

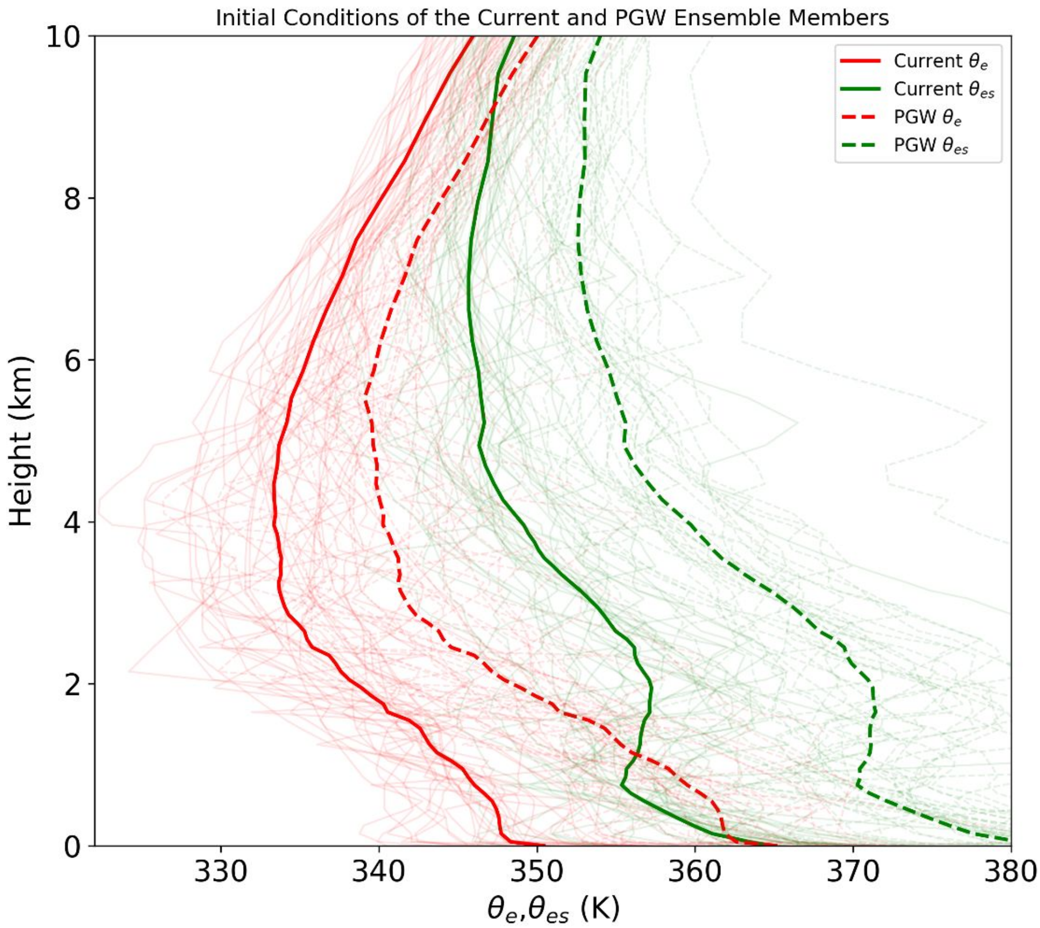

Fig. 2 The initial profiles of equivalent potential temperature and saturated equivalent potential temperature for the current and PGW scenarios. Solid lines represent the current scenario, and dashed lines represent the PGW scenario. Red lines indicate equivalent potential temperature, and green lines indicate saturated equivalent potential temperature. Thick lines represent the mean initial soundings, while thin lines represent 30 initial soundings. In Current and the PGW scenario, the mean lifting condensation level (LCL) are both 960 hPa, level of free convection (LFC) are 820 and 840 hPa. The convective inhibition (CIN) are 55 and 45 Jkg^{-1}, and the convective available potential energy (CAPE) are 1600 and 3200 Jkg^{-1}, respectively.

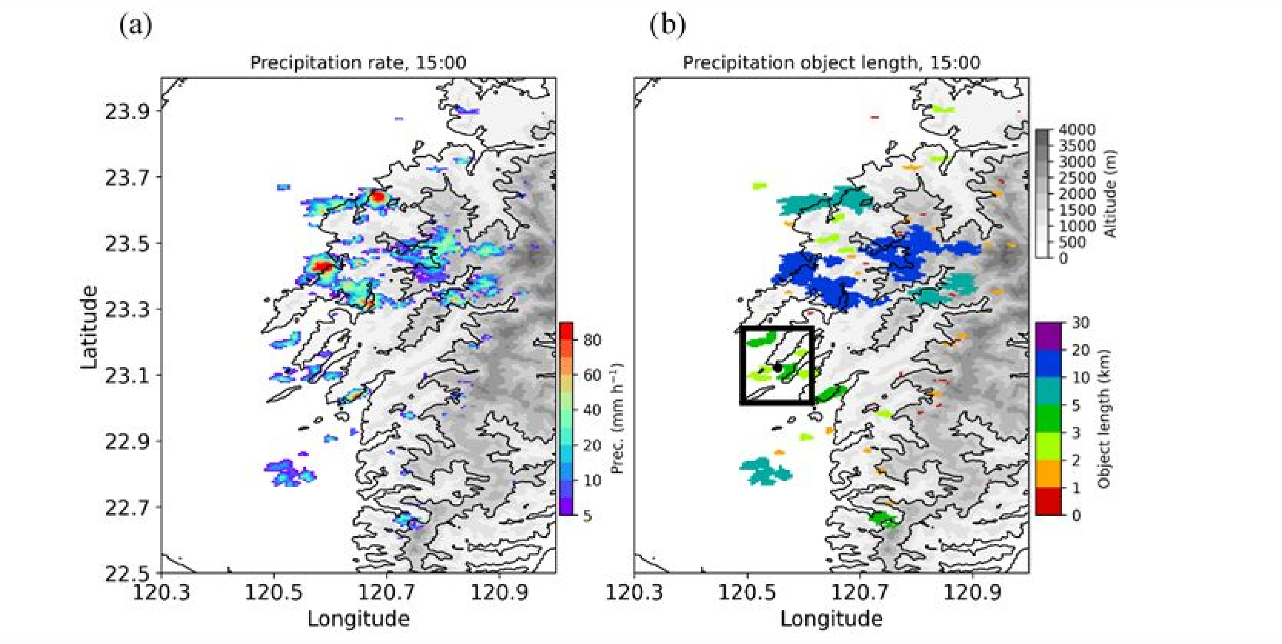

Fig. 3 Schematic diagram of the precipitation object length. (a) shows a color-shaded snapshot of the precipitation rate in the mountainous region for one ensemble member during the afternoon, while (b) shows the corresponding snapshot of the precipitation object length at the same time. The grey shading represents the terrain, with black contours indicating altitudes of 0, 500, and 1500 meters. The edge length of the black box represents the environmental scale (approximately 10 km), based on three times the 75th and 90th percentile of the precipitation object length at the same time and for the same ensemble member. The value of $\tilde{\theta}_v$ is the horizontally averaged potential temperature within the black box region, centered at the black point.

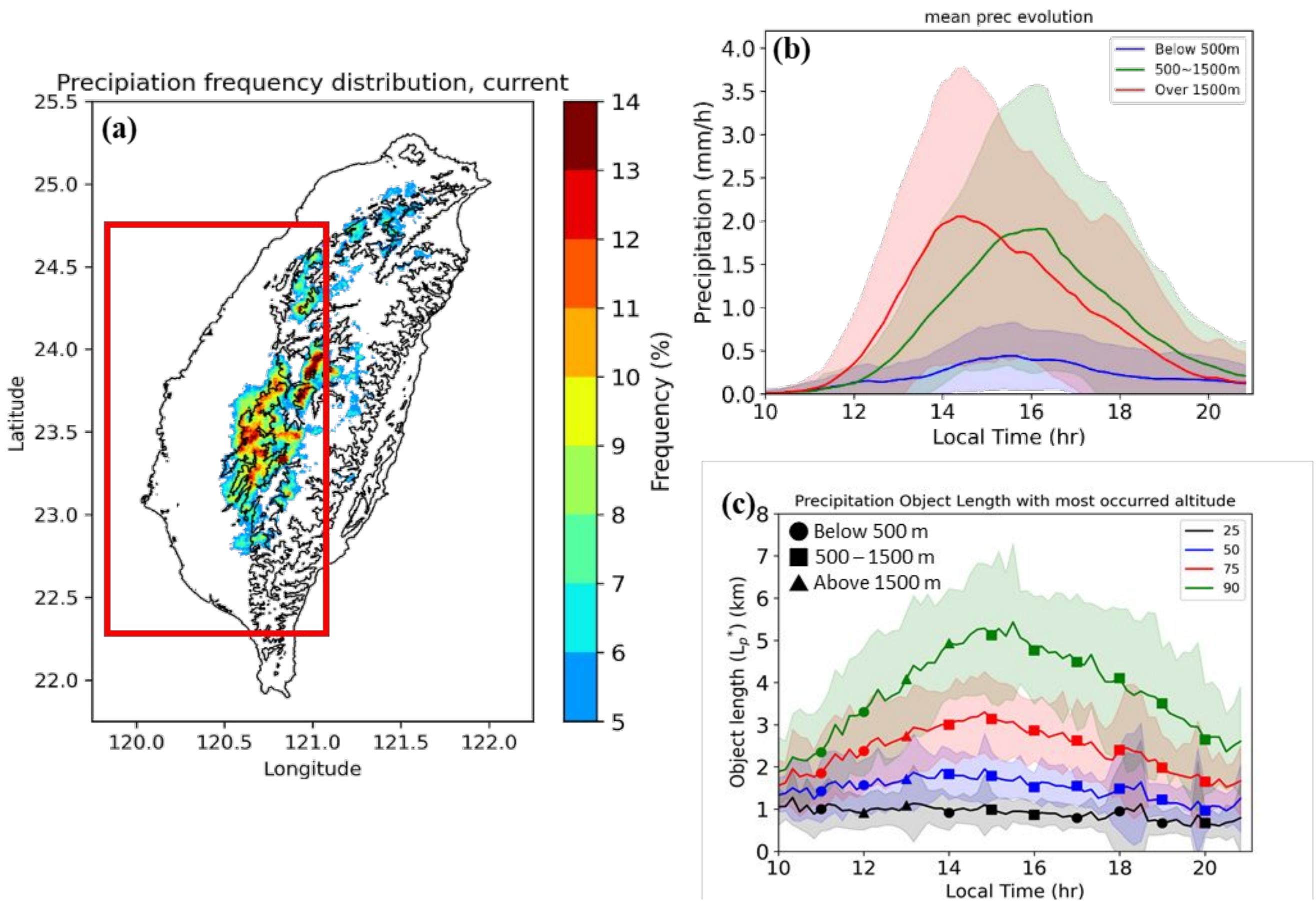

Fig. 4 (a) The frequency (%) of precipitation exceeding 5 mm h⁻¹ (shaded), based on statistics from 14 to 21 LST across 30 ensemble members. Black contours represent altitudes of 0, 500, and 1500 meters. The red box highlights the study region with relatively high precipitation frequency. (b) The precipitation evolution in three sea-level height regions (below 500 m, 500–1500 m, and above 1500 m) within the red box from (a). The line represents the mean, and the shaded area indicates one standard deviation of precipitation across 30 ensemble members. (c) The evolution of precipitation object length over four percentiles (25th, 50th, 75th, 90th) per time period for each ensemble member. The line represents the mean, and the shaded area indicates one standard deviation of precipitation object length across 30 ensemble members. The markers indicate different sea-level height regions where the mode of precipitation object centers falls within the four percentiles across all 30 ensemble members. Dots represent areas below 500 m (plain), squares correspond to regions between 500 and 1500 m (mountain hill region), and triangles denote areas above 1500 m (high-mountain region).

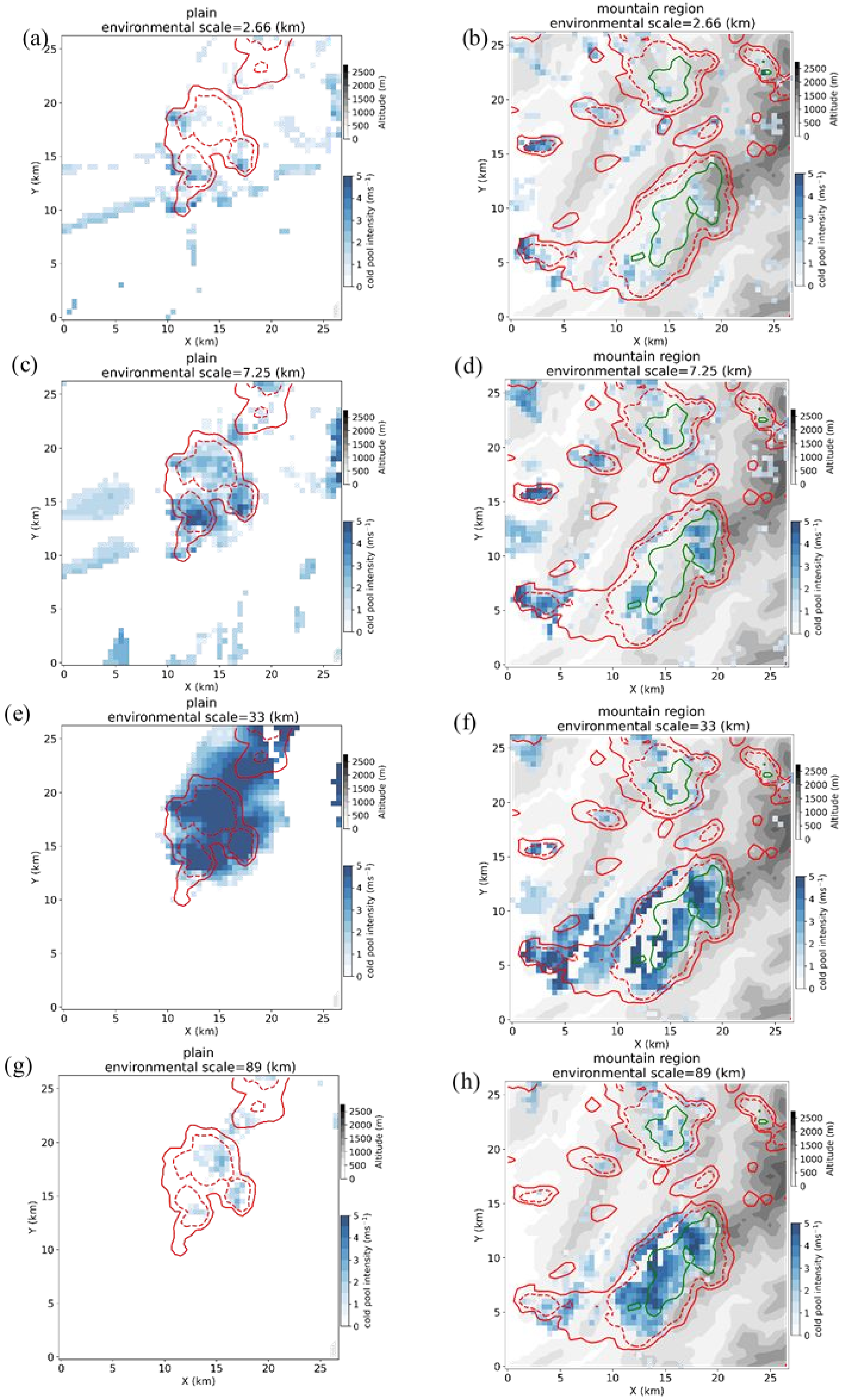
(a)
plain
environmental scale=2.66 (km)
(b)
mountain region
environmental scale=2.66 (km)
(c)
plain
environmental scale=7.25 (km)
(d)
mountain region
environmental scale=7.25 (km)
(e)
plain
environmental scale=33 (km)
(f)
mountain region
environmental scale=33 (km)
(g)
plain
environmental scale=89 (km)
(h)
mountain region
environmental scale=89 (km)
X (km)
Y (km)
Altitude (m)
cold pool intensity (ms⁻¹)

Fig. 5 The precipitation at rates of 5, 15, and 50 mm h^{-1} (red solid, red dashed, and green solid contours, respectively) and cold pool intensity (blue shading, unit: m s^{-1}) calculated using different environmental scales in the plain (a, c, e, g) and mountainous (b, d, f, h) regions for one ensemble member. Grey shading represents sea-level height (in meters).

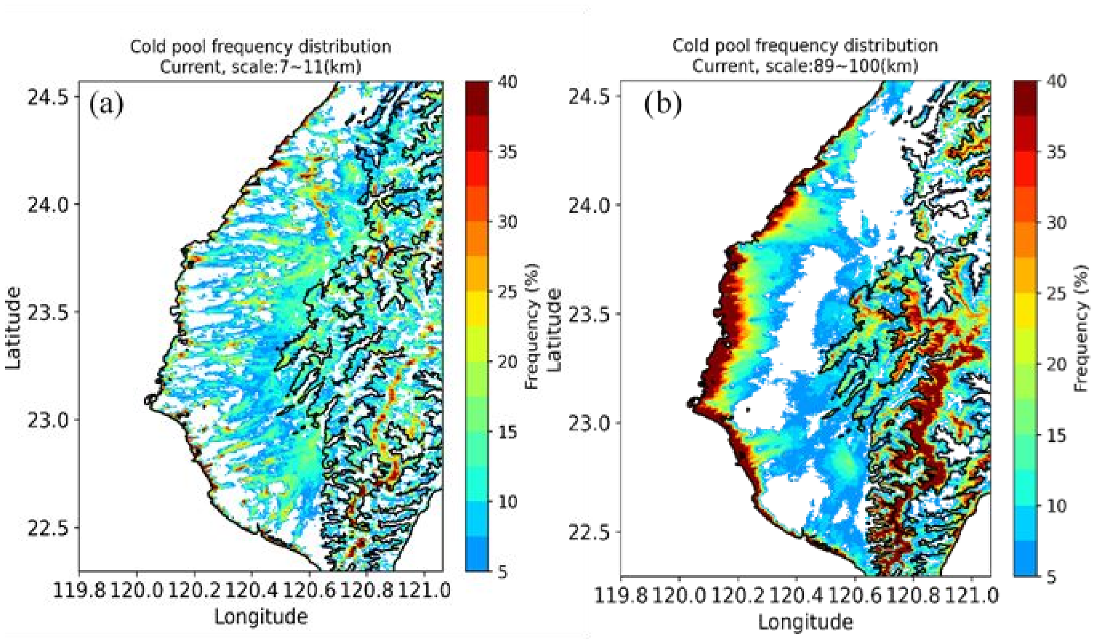

Fig. 6 The occurrence frequency map of cold pools under the appropriate environmental scale of (a) 7–11 km and (b) 89–100 km during 14–21 LST. Frequency is defined by the number of occurrences where cold pool intensity is ≥ 1 m s^{-1}. Contours represent altitudes of 0, 500, and 1500 meters.

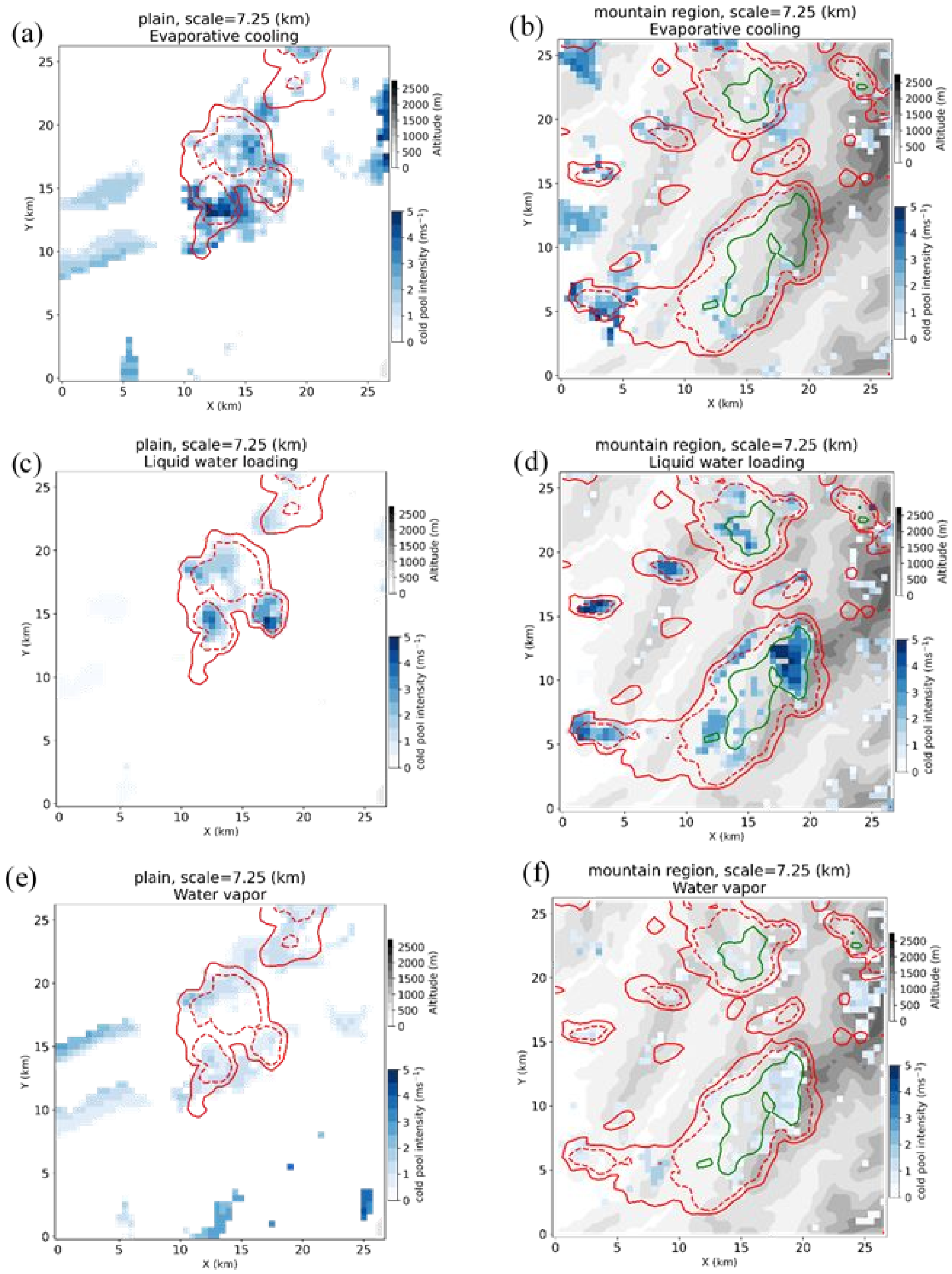

Fig. 7 The negative buoyancy contribution to the cold pool, under the appropriate environmental scale (7–11 km, represented here by a scale of 7.25 km), is shown in Figs. 5c and 5d for the plain (a, c, e) and mountainous (b, d, f) regions. Panels (a, b), (c, d), and (e, f) correspond to the contributions from evaporative cooling, increased liquid water content loading, and reduced water vapor effects, respectively. Precipitation rates of 5, 15, and 50 mm h^{-1} are shown with red solid, red dashed, and green solid contours,

respectively, while cold pool intensity is shown in blue shading (unit: m s⁻¹). Grey shading represents altitude (in meters).

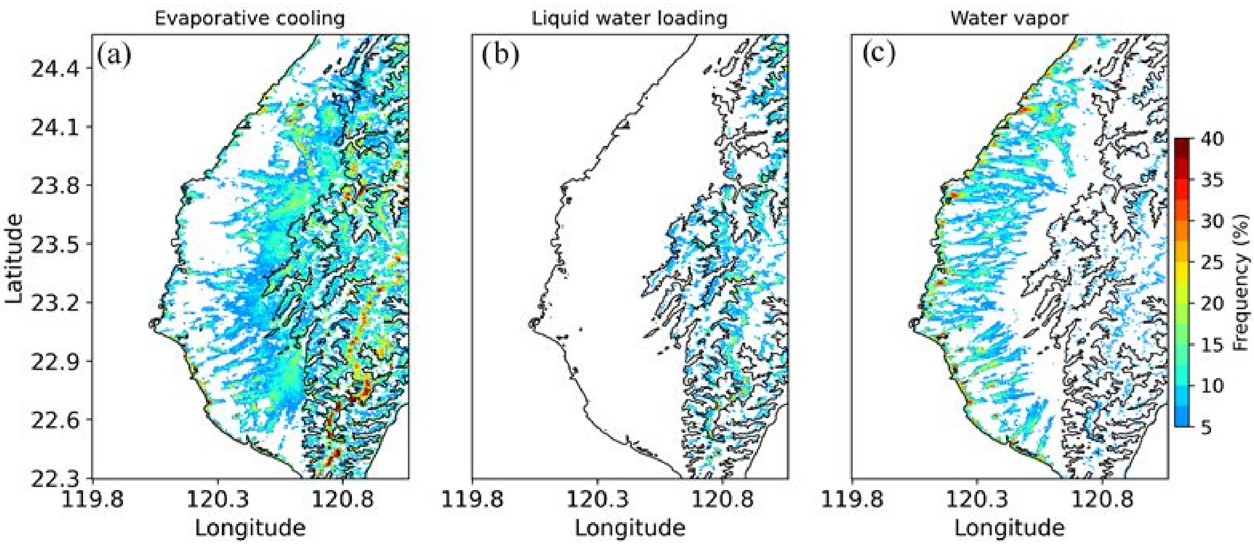

Fig. 8 The occurrence frequency map of cold pools driven by negative buoyancy contributions from (a) evaporative cooling, (b) increased liquid water loading, and (c) reduced water vapor under the appropriate environmental scale (7–11 km) during 14–21 LST. Frequency is defined by the number of occurrences where cold pool intensity is ≥ 1 m s⁻¹. Contours represent altitudes of 0, 500, and 1500 meters, respectively.

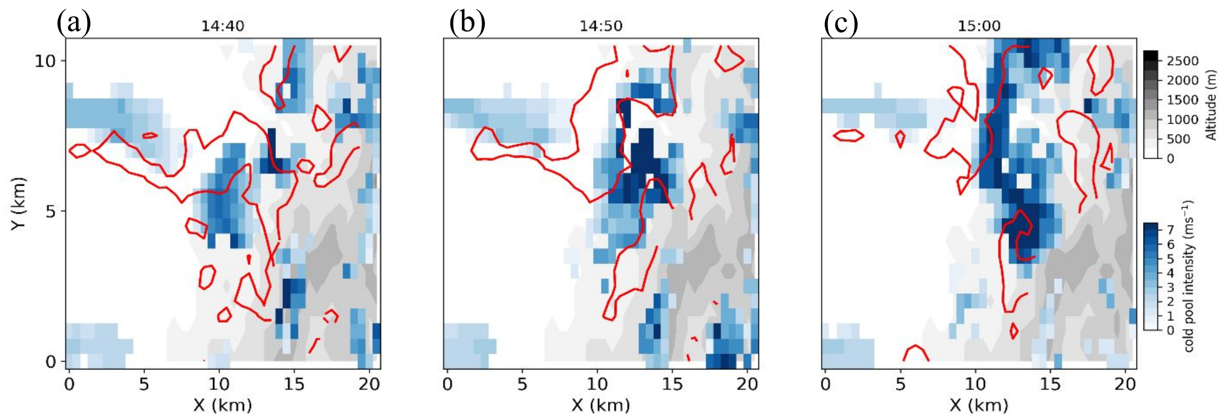

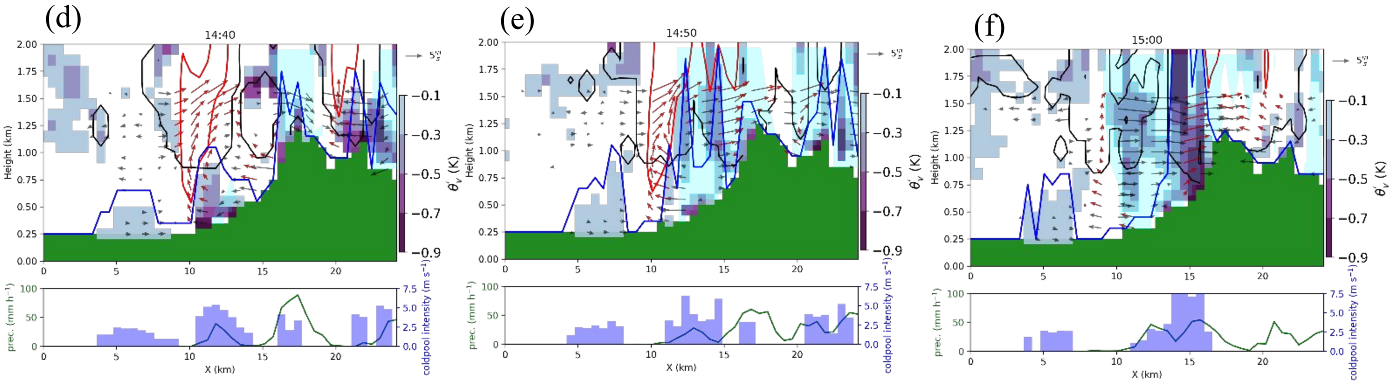

Fig. 9 The evolution of the horizontal (a–c) and vertical cross-section (d–f) from 14:40 to 15:00 LST with the cold pool calculated using the 7–11 km environmental scale. In the upper panel (a–c), grey shading represents sea-level height (m), blue shading shows cold pool intensity (m s⁻¹), and the red contour marks the updraft region where vertical velocity is 1 m s⁻¹ at a 1 km height. In the lower panel (d–f), the vertical cross-section follows the black dashed line in (a–c), oriented from Northwest to Southeast. In the upper portion of (d–f), green bars represent terrain height (km), blue line indicates cold pool height (km), purple shading denotes the negative θ'_v, which is $(\theta_v - \tilde{\theta}_v)$ (K). Black contour represents where the combined cloud water and ice water mixing ratio higher than 0.01 g kg⁻¹, and bright shading highlights rainwater regions where the mixing ratio exceeds 0.5 g kg⁻¹. Purple vectors represent the horizontal wind anomaly, calculated by subtracting the horizontal wind at X = 0 km (sea-breeze inflow) from the original wind field, and are projected along the dashed line. These vectors are combined with vertical wind (m s⁻¹), while red vectors highlight vertical winds exceeding 1 m s⁻¹. The red contour represents a region where the updraft velocity is higher than 3 m s⁻¹. In the lower portion, blue bars depict cold pool intensity (m s⁻¹), and the green line represents precipitation rate (mm h⁻¹).

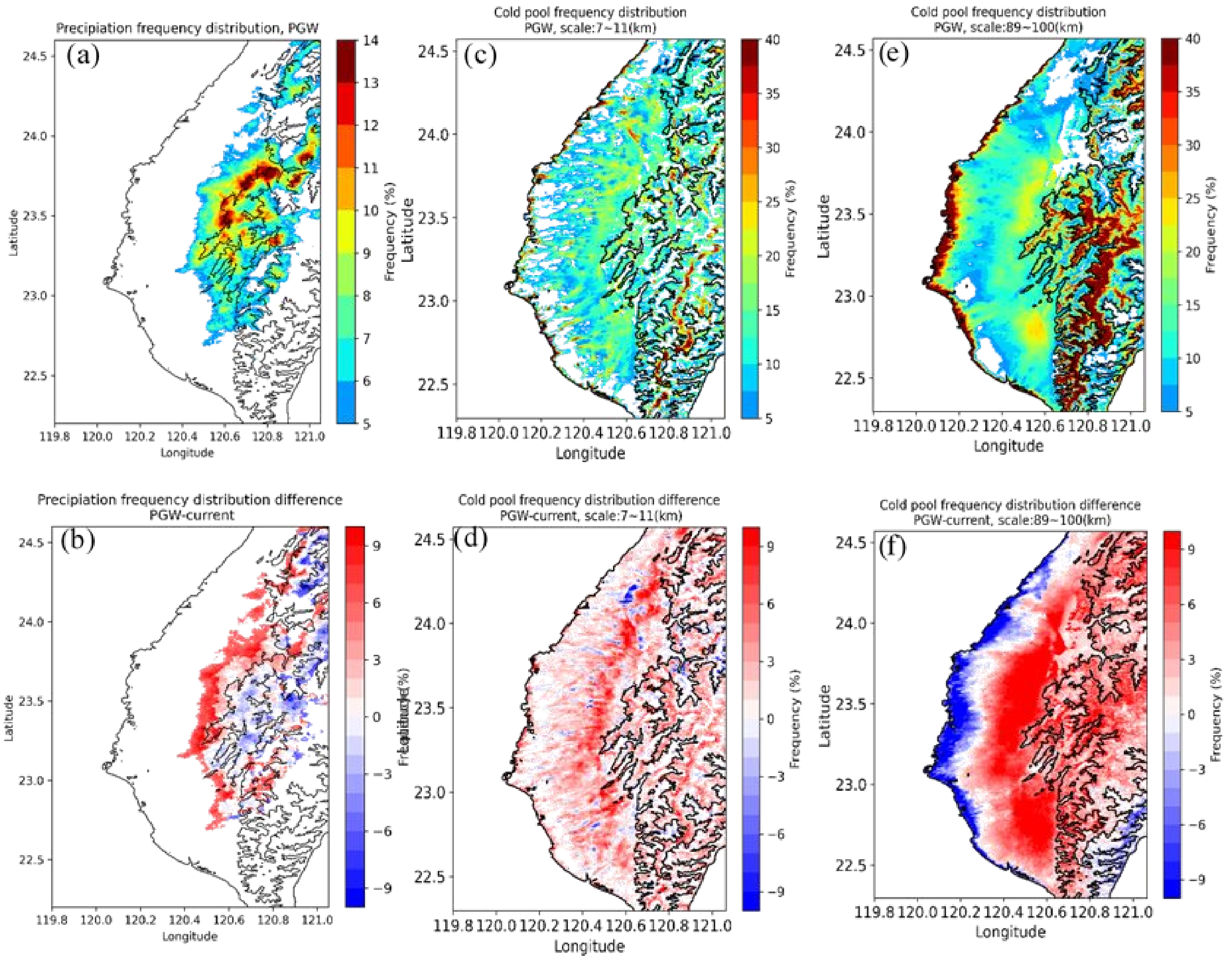

Fig. 10 The occurrence frequency map from 14:00 to 21:00 LST for precipitation (a, b) and cold pools under environmental scales of 7–11 km (c, d) and 89–100 km (e, f) in the PGW scenario, along with the difference between the two scenarios (PGW - current). Frequency is defined by the number of occurrences where cold pool intensity is ≥ 1 m s^{-1}. Black contours represent altitudes at 0, 500, and 1500 meters, respectively.

List of Tables

Table 1 Configuration of the TaiwanVVM for semi-realistic simulations under current and Pseudo Global Warming (PGW) scenarios.

Domain size (grid points)	512 km * 512 km * 19260 m 1024 * 1024 * 70 grids
Horizontal resolution	500 m
Vertical resolution	100 m (< 3900 m) Stretch up to 955 m (3900 m ~ model top)
Time step	10 secs
Simulation duration	24 h (00:00 ~ 24:00)
Lateral boundary condition	Double periodic
Output frequency	10 mins
PGW scenario	Temperature + 3K Keeps the same Relative Humidity

Identifying Cold Pool scales over Complex Topography using TaiwanVVM simulations

We sincerely appreciate the editors' careful evaluation and constructive suggestions. In response to the editors' feedback, all changes have been accepted, and the final version is clean without any revision marks. Additionally, we have made a comprehensive revision to clarify our approach to defining the environmental scale over Taiwan's complex topography. Additionally, we have refined the manuscript to ensure clarity, incorporating input from English editing experts.